Electronic Supplementary Material (ESI) for Nanoscale.
This journal is © The Royal Society of Chemistry 2019

Supporting information for

Interfacial THz generation from graphene/Si mixed-dimensional van der Waals heterostructure

Zehan Yao[a], Yuanyuan Huang[a], Lipeng Zhu[c], Petr A. Obraztsov*[b], Wanyi Du[a], Longhui Zhang[a], Xinlong Xu*[a,d]

[a]a. Shaanxi Joint Lab of Graphene, State Key Lab Incubation Base of Photoelectric Technology and Functional Materials, International Collaborative Center on Photoelectric Technology and Nano Functional Materials, Institute of Photonics & Photon-Technology, Northwest University, Xi'an 710069, China.

b. A. M. Prokhorov General Physics Institute, RAS, Moscow, Russia.

c. School of Electronic Engineering, Xi'an University of Posts and Telecommunications, Xi'an 710121, China.

d. Guangxi Key Laboratory of Automatic Detecting Technology and Instruments, Guilin University of Electronic Technology, Guilin 541004, People's Republic of China

*Corresponding author, E-mail: p.obraztsov@gmail.com (Petr A. Obraztsov) or xlxuphy@nwu.edu.cn (Xinlong Xu).

S1. Details of the device structure and fabrication processes.

The transfer procedure was done as quickly as possible in air to avoid the thick native oxide layer. After 5% HF treatment for 15 s, graphene was immediately transferred onto the Si surface. The post-transferred sample was then dried in 60°C for 30 min. Native oxide layer with thickness of ~ 0.2 nm would form on bare Si (doping density 8×10^{11} cm^{-3}) after exposing to air and ultrapure water for several tens of minutes during the transfer process[1].

The details of device structure are shown in Figure S1. Two metal ring electrodes were patterned at the front and back side of the sample respectively to apply the gate voltage to the interface layer. At the front side (Figure S1a), graphene was first transfer to Si substrate (Figure S1b). An insulating ring was coated on the sample surface as shown in Figure S1c, before the metal ring depositing on graphene surface (Figure S1d). Therefore, the insulating ring was located between metal electrode and Si surface to prevent the formation of metal/Si interface, which introduces charge transport between metal and Si. The insulating ring is made by polyacrylate with a thickness of approximately 10 μm.

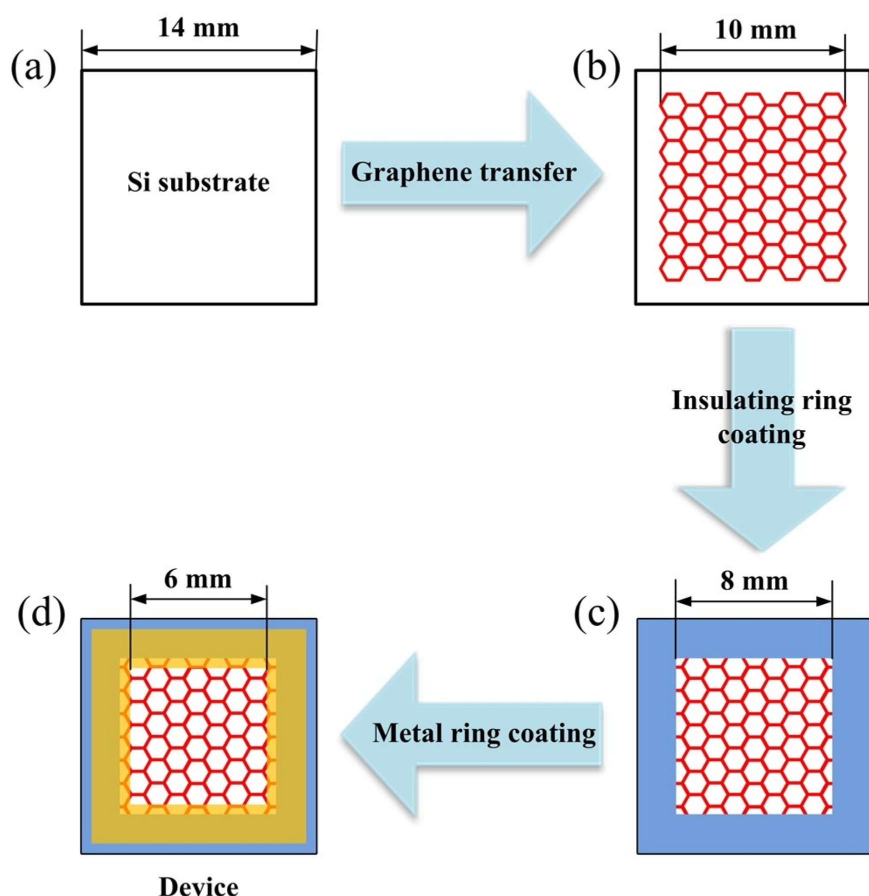

Figure S1 Fabrication of the graphene/Si THz emitter. Graphene was transferred onto (a) the Si substrate to form (b) graphene/Si heterostructure. (c) Consequently, insulating ring was fabricated onto the sample surface before (d) the metal ring coating to prevent the contact of metal ring with Si substrate.

S2. Raman and visible-infrared spectroscopy of graphene.

The quality of graphene film was characterized by Raman spectrum and visible-near infrared spectrum. The amplitude of 2D mode at 2700 cm^{-1} is two times larger than that of G mode at 1583 cm^{-1}, and D mode at 1351 cm^{-1} is nearly absent (Figure S2a). These results suggest a high quality of single layer graphene with low defect density. The visible-near infrared absorption is approximately 2.3% (Figure S2b), which also suggests that the graphene sample is a single layer graphene.

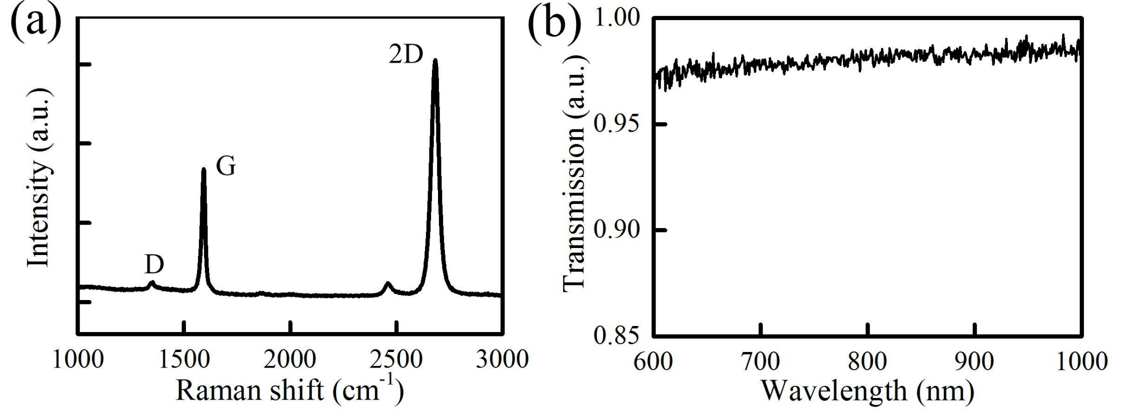

Figure S2 (a) Raman spectrum of single layer graphene excited by a 532 nm laser. (b) Visible-near infrared spectrum for graphene on a quartz substrate, demonstrating an approximate 97.5% transmission from 600 nm to 1000 nm.

S3. THz emission in transmission configuration

THz emission from graphene/Si Schottky junction (GSSJ) was measured in a transmission configuration as shown in Figure S3a. The p-polarized THz emission amplitude depends on the incident angle θ_{in} as shown in Figure S3b, which can be fitted by:

$$E(\theta_{in}) \propto \sin(\theta_{in})[1-(\frac{\tan(\theta_{in}-\theta_2)}{\tan(\theta_{in}+\theta_2)})^2]\times\frac{2\cos(\theta_{in})\sin(\theta_2)}{\sin(\theta_{in}+\theta_2)\cos(\theta_{in}-\theta_2)}, \quad \text{(S1)}$$

where $\theta_2 = \sin^{-1}[\sin(\theta_{in})/n_2)]$ and n_2 is the silicon refraction index in THz region. THz emission cannot be detected at normal incidence, suggesting the emitted THz E-field component is perpendicular to the sample surface.

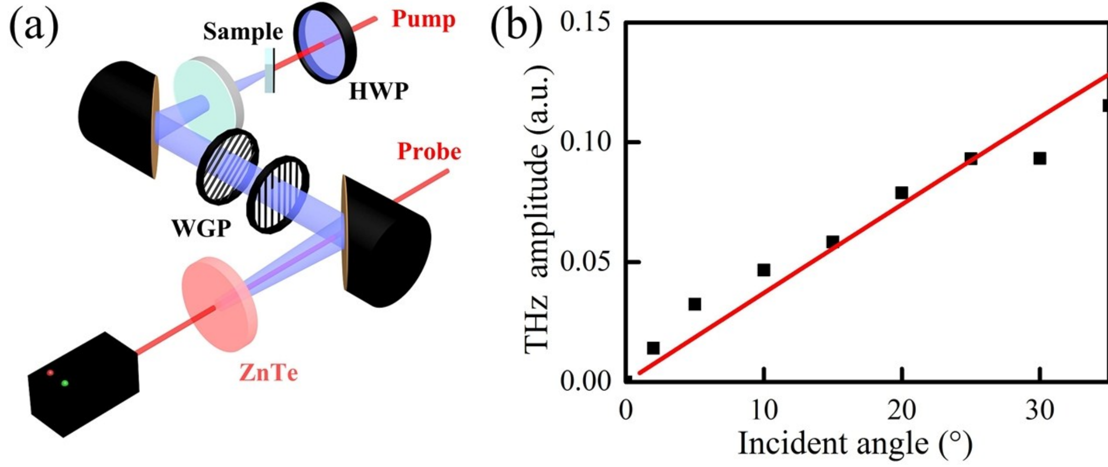

Figure S3 (a) Schematic of THz emission spectroscopy in a transmission configuration. P1 is the THz wire-grid polarizer. (b) THz emission amplitude with respect to the incidence angle. Dots are the experimental results and curves are the fitting result.

S4. Photocarrier dynamics in GSSJ of THz generation

The photocarrier dynamics can be described via drift-diffusion equation[2]:

$$\frac{\partial N(z,t)}{\partial t} = D(z,t)\frac{\partial^2 n(z,t)}{\partial z^2} \pm \frac{\partial}{\partial z}\left[\mu(z,t)n(z,t)E(z,t)\right] + G\left(z,t\right), \tag{S2}$$

$$E_{THz} \propto \int \frac{\partial J}{\partial t}dz \propto \int \frac{\partial^2 n(z,t)}{\partial t^2}dz\ , \tag{S3}$$

where n refers to the carrier concentrations; E is the electric field, G refers to the photoexcitation term; J is the photocurrent; $\mu = v_{drift} / E(z,t)$ is the carrier mobility and v_{drift} is the drift velocity. The diffusion constant is $D = k_B T \mu / e$, where k_B refers to Boltzmann constant and T is the temperature. The rising time of photocarrier generation/acceleration is within femtosecond timescale, which is dominated by the pump laser duration (G in S2). The decay time of photocarrier generation/acceleration is within several to tens of picosecond timescale (μ and D in S2). As indicated in Equation (S2-S3), the total temporal THz response is dominated by the carrier drift velocity v_{drift} and photocarrier generation term G. Drift velocity

v_{drift} determined the carrier mobility μ and diffusion constant D, while photocarrier generation term G determined the photocarrier density n. Therefore, the photocurrent can be defined as[3] $J = nev_{drift}$.

S5. Comparison of THz emission from GSSJ and GaAs (100).

Comparison of THz emission from GSSJ and GaAs (100) is shown in Figure S4 (a-b). Without applying gate voltage (V_g), THz emission from GSSJ is smaller than that from GaAs (100) at pump fluence from 1.4 μJ/cm^2 to 15.5 μJ/cm^2. This is mainly due to the lower drift velocity and lower photocarrier density. We illustrate the drift photocarriers on Si surface (Figure S4 c) and GaAs surface (Figure S4 d) to understand the low photocarrier density from Si surface. The electric field at the interface depletion layer is expressed as:[4] $E(z) = qN_d(z - z_d)/\varepsilon_r\varepsilon_0$, where N_d is the doping concentration; ε_r is the dielectric constant of the semiconductor. The depletion layer width z_d can be defined as $z_d = \sqrt{-2\varepsilon_r\varepsilon_0\varphi_d/qN_d}$, where φ_d is the build-in electric potential of depletion layer. We consider the same electric field distribution on Si and GaAs surface. For 800 nm excitation beam, the absorption coefficient α on Si surface is 850 cm^{-1} [5], which is much less than that on GaAs surface (13980 cm^{-1})[6]. As a result, the photogenerated charges on Si surface (Figure 2c) are much less than that on GaAs surface (Figure 2d). Moreover, the absorption length ($\Delta = 1/\alpha$) is 11.7 μm on Si surface for 800 nm excitation, which is much longer than that on GaAs surface (720 nm). For N_d=8×10^{11} cm^{-3} and $|\varphi_d|$<0.09 V, the depletion width z_d on Si surface is shorter than the absorption length. The photocarriers generated outside the surface depletion region have no contribution to the transient drift current. Hence, photocarrier density on Si contributes to the transient drift photocurrent is significantly lower than that on GaAs. For Si is n-type with doping density of 8×10^{11} cm^{-3}, while the GaAs is n-type without doping, the depletion layer at GSSJ interface was wider and the built-in electric field would be larger than that at GaAs surface. Hence, though the GaAs is 20x better in absorbing 800-nm light with

much larger mobility than Si, THz emission amplitude from GSSJ without applying V_g is still comparable to that from GaAs.

Under large reverse V_g, the width of the depletion layer is wider than the absorption length. Since the absorption coefficient in Si is 11.7 μm, the interface built-in potential is needed to be larger than 0.09 V. According to our previous study[7], built-in potential at graphene/SiO_2/Si interface was enhanced more than 0.09 V by varying the applying gate voltage from 2 V to -2 V. Therefore, width of the GSSJ depletion layer would be larger than the absorption length when applying gate voltage with several volts. In this case, all the photocarriers generated in the depletion layer can make a contribution to the transient drift current.

Figure S4b shows the pump fluence dependent THz generation from GSSJ and GaAs. The experimental results can be fitted by a transient photocurrent based saturation model:[8]

$$E_{THz}^{pk} = (AF)/(F + F_{sat}), \quad \text{(S4)}$$

where A is related to the THz emission intensity; F is the pump fluence; F_{sat} is the saturation pump fluence. The saturation was caused by the screening effect due to the high density of photocarriers. The results of GaAs and GSSJ without applying reverse V_g are fitted well with the F_{sat}, which are 4 μJ/cm^2 and 7.5 μJ/cm^2, respectively. Under -5 V V_g, the THz generation can be fitted well with Equation (S4) as F_{sat}=14 μJ/cm^2.

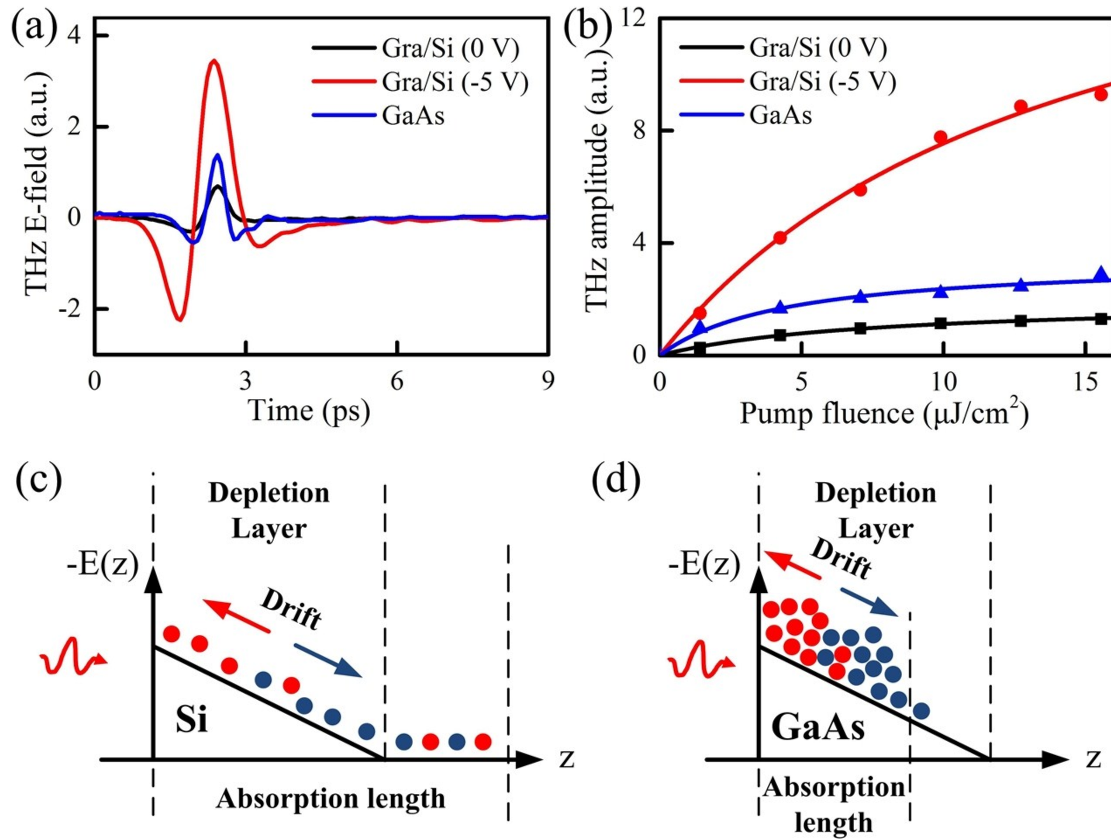

Figure S4 (a) Comparison of THz generation from GSSJ and GaAs (100) at 7 μJ/cm^2 pump fluence. (b) Pump fluence dependent THz generation from GSSJ and GaAs. Dots are the experimental results and curves are the fitting results. (c-d) Illustration of electric field distribution and drift photocarriers on Si and GaAs surfaces. The red and blue circles refer to positive and negative charges respectively.

S6. Impact of applying positive V_g on THz emission from GSSJ

The applying positive V_g would decrease the built-in electric field at the interface, and thus reduce the THz emission amplitude as shown in Figure S5a. The decreasing THz emission amplitude as shown in Figure S5b reach a saturation without polarity flipping, which is due to the Si bulk resistance eliminates the bias effect on the interface layer. This saturation has been observed at graphene/SiO_2/Si interface[7] and metal/Si interface[9].

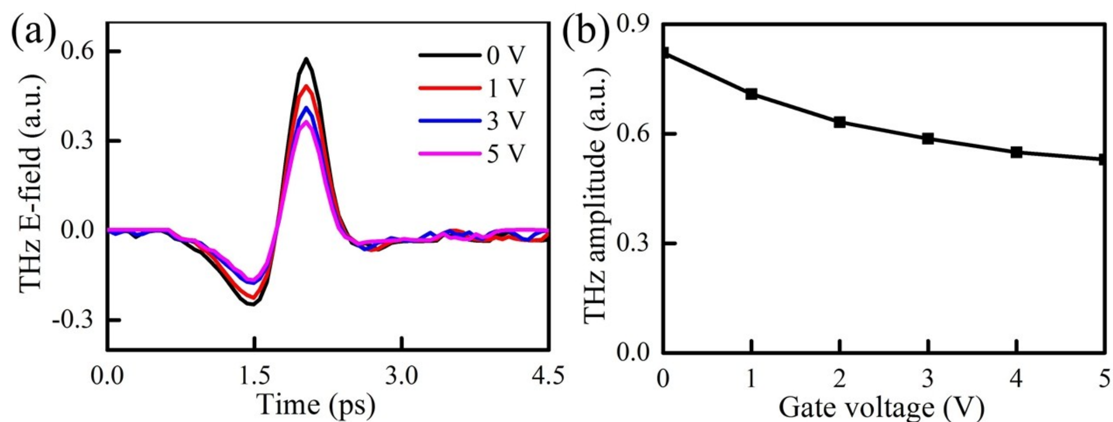

Figure S5 (a) Emitted THz signal from GSSJ under positive V_g. (b) THz emission amplitude as a function of positive V_g.

S7. Impact of HF etching on Si

Graphene was transferred onto post-HF-etched Si in air condition, and dried at 60°C for 30 min. According to the previous study, native oxide layer with thickness of ~ 0.2 nm would formed on bare Si (doping density 8×10^{11} cm^{-3}) after exposing to air and ultrapure water for several tens of minutes during the transfer process[1]. However, we give the direct evidence that most of the oxide layer was removed after the HF treatment. As shown in Figure S6, HF treatment significantly reduces the THz emission amplitude from Si surface. This is because the effective reduction of oxide thickness removes the oxygen adsorbates induced surface electric dipole, which modified the built-in electric field[10]. The effective reduction of oxide thickness also facilitate the tunnelling current from the outermost Si surface through the ultrathin oxide layer under gate voltage, which in turn disable the charge accumulation in the inversion layer. As a result, THz emission amplitude can be improved without saturation by applying gate voltage.

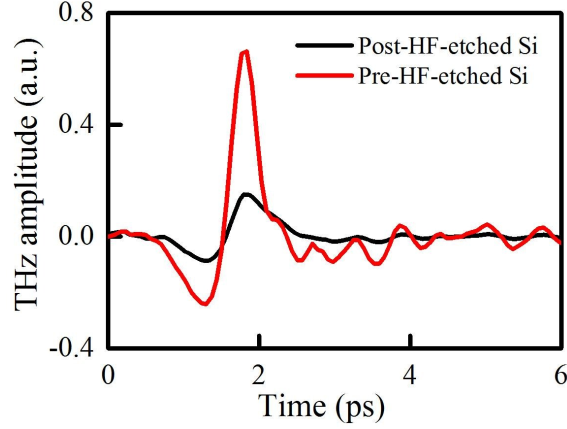

Figure S6 THz emission from post-HF-etched Si and pre-HF-etched Si.

S8. Pump polarization angle dependent THz emission.

THz emission amplitude with respect to pump polarization angle as shown in Figure S7 can be fitted by $E^{THz} = C_{EFIOR}\sin 2\theta + C_{current}$, where C_{EFIOR} corresponds to the magnitude of optical rectification depending on the pump polarization angle θ; $C_{current}$ is related to the transient photocurrent, which is independent of θ. The fitting results indicate that the contribution of EFIOR effect is approximately 21 times larger than that of transient photocurrent under both 0 V (Figure S7a) and -40 V V_g (Figure S7b). These results show the same enhanced factor of 26 at 7 μJ/cm^2 excitation for both EFIOR and transient photocurrent effect under reverse V_g compare with that without applying V_g. THz E-field generated by transient photocurrent can be expressed by $E^{THz} \propto \int \frac{\partial J}{\partial t} dz = ne\mu \int E(z)dz$, where *E(z)* is the built-in electric field and $\int E(z)dz = \varphi_d$. Hence, THz amplitude linearly depend on the depletion potential φ_d. Since both the EFIOR and transient photocurrent induced THz emission amplitude is proportional to the built-in potential at the depletion case[7, 11], we come to a conclusion that the interface built-in potential was enhanced by 26 times.

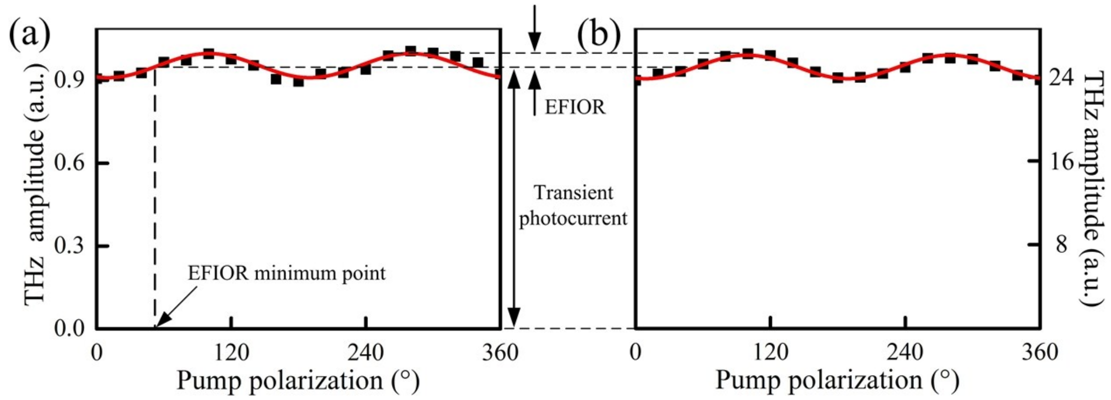

Figure S7 Pump polarization angle dependent THz emission amplitude from GSSJ under (a) 0 V V_g and (b) -40 V V_g at 7 μJ/cm^2 excitation.

S9. Pump dependent THz generation from GSSJ and InAs (100).

The pump fluence dependent THz generation form GSSJ without applying V_g and InAs are fitted by the Equation (4) in the main text as shown in Figure S8. The fitting results suggest the F_{sat} for GSSJ (0 V) and InAs are 7.5 μJ/cm^2 and 13.5 μJ/cm^2, respectively.

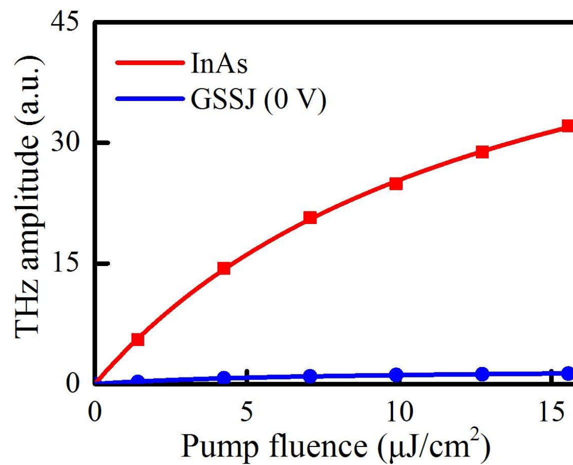

Figure S8 Pump fluence dependent THz generation from GSSJ (0 V) and InAs. The dots are experimental results and curves are fitting results.

S10. THz signal in frequency domain from GSSJ

Mechanism of THz emission from GSSJ is similar to that from photoconductive antennas, as both of them result from the free carrier acceleration under electric field. Hence, the emitted THz bandwidth from GSSJ is limited by the finite carrier lifetime[12] and the depletion layer width. Carrier lifetime in silicon (nano- to microsecond) is much longer than THz pulse duration (picosecond), and thus shows negligible impact on the emitted THz bandwidth under ambient gate voltage. While the depletion layer width at graphene/Si interface is more than 1 micrometer[13], which is comparable to the typical THz wavelengths. As shown in Figure S9 (a-c), the emitted THz bandwidth from GSSJ is similar until -5 V. However, the emitted THz bandwidth is reduced under -40 V gate voltage as shown in Figure S9 (d). This is due to the reason that the depletion region will be significantly broadened when large gate voltage is applying on the interface, which is similar to THz emission from photoconductive antenna as a longer antenna length for narrower THz bandwidth[14].

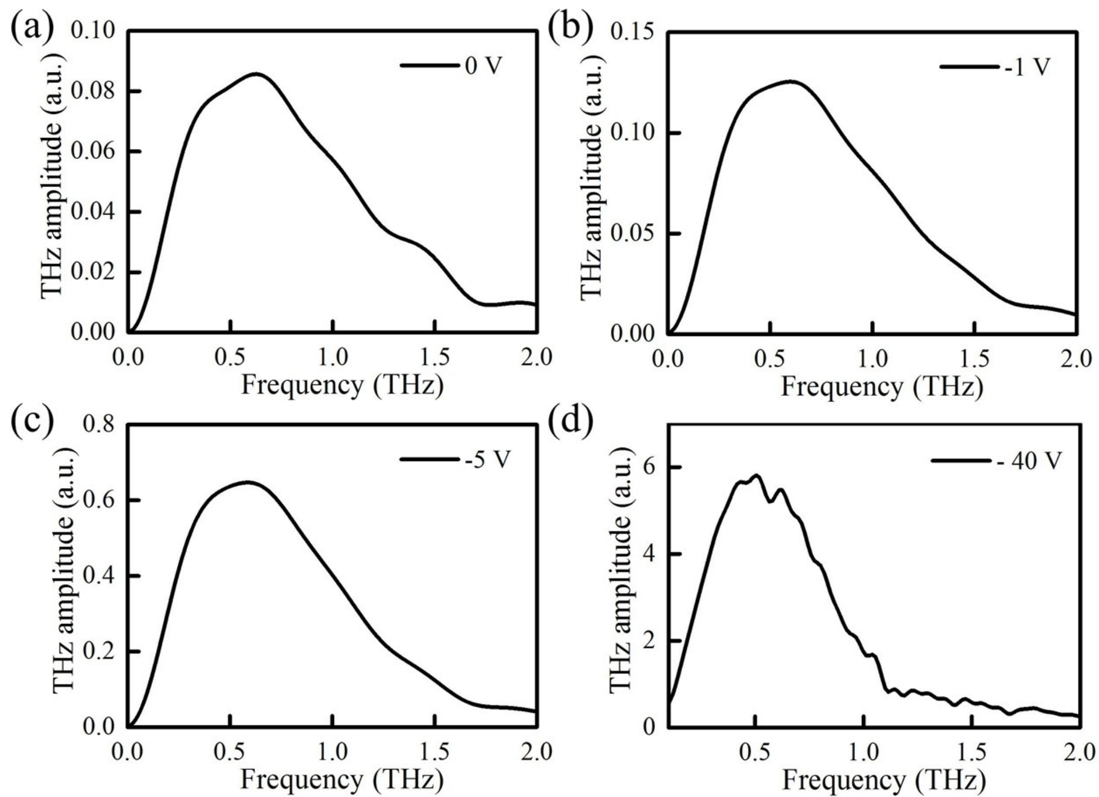

Figure S9 Generated THz signal from GSSJ at frequency spectrum at V_g = (a) 0 V, (b) -1 V, (c) -5 V, and (d) -40 V.

S11. Stability of GSSJ THz emitter

The GSSJ THz emitter was exposed to 42 μJ/cm^2 laser (800 nm femtosecond pulse laser) illumination at V_g=-40 V for 30 minutes and emitted unchanged THz signal as shown in Figure S10, which suggests a good working stability.

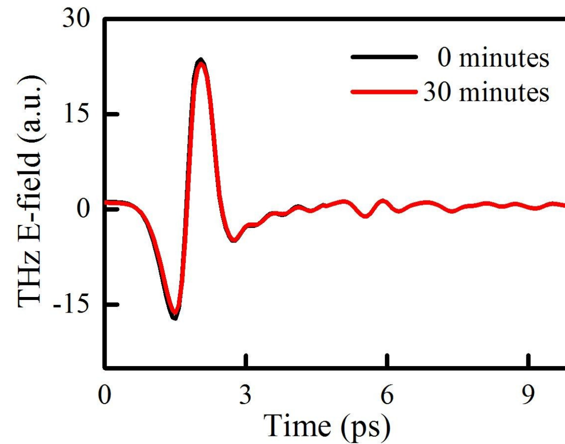

Figure S10 THz emission from GSSJ before (black) and after (red) exposed at 15.6 μJ/cm^2 excitation and -40 V V_g for 30 minutes.

S12. THz peak-to-valley amplitude VS. entire frequency spectrum area.

We extract the pump fluence dependent THz emission amplitude by peak-to-valley value (Figure S11a) and entire frequency spectrum area (Figure S11b) to check the method of using THz peak-to-valley amplitude. The fitting results by the Equation (4) in the main text indicate the same fluence threshold, which demonstrate that the peak-to-valley value used in our manuscript is appropriate.

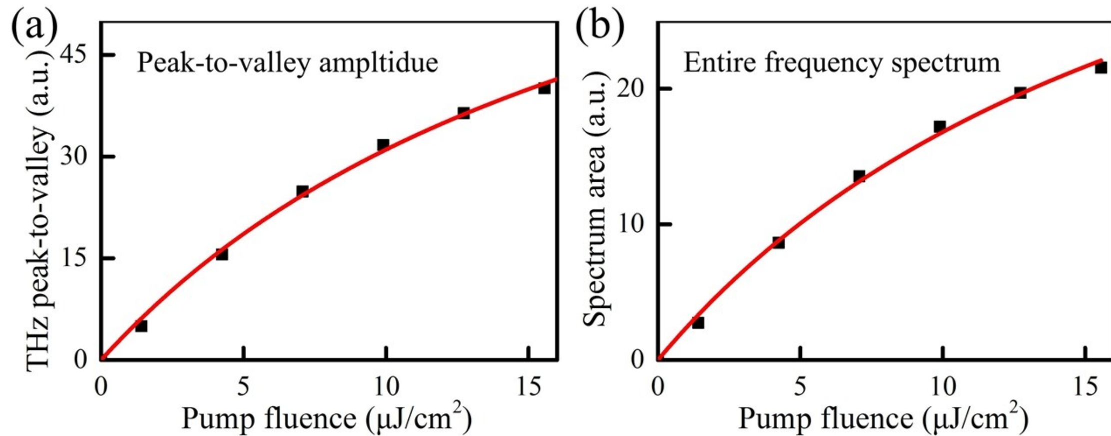

Figure S11 Comparison of the emitted THz signal from GSSJ in (a) peak-to-valley amplitude and (b) entire frequency spectrum area. Plots are the experimental results and curves are the fitting results.

References

1 M. Morita, T. Ohmi, E. Hasegawa, M. Kawakami and M. Ohwada, *Journal of Applied Physics*, 1990, **68**, 1272-1281.

2 K. Liu, J. Xu, T. Yuan and X. C. Zhang, *Physical Review B*, 2006, **73**, 155330.

3 C. Jacoboni and L. Reggiani, *Reviews of Modern Physics*, 1983, **55**, 645-705.

4 S. M. Sze and K. K. Ng., *Physics of semiconductor devices*, John wiley & sons, America, 2006.

5 G. M. A. and K. M. J., *Progress in Photovoltaics: Research and Applications*, 1995, **3**, 189-192.

6 G. E. Jellison Jr, *Optical Materials*, 1992, **1**, 151-160.

7 Z. Yao, L. Zhu, Y. Huang, L. Zhang, W. Du, Z. Lei, S. Ajay and X. Xu, *ACS Applied Materials & Interfaces*, 2018, **10**, 35599-35606.

8 M. Reid and R. Fedosejevs, *Applied Physics Letters*, 2005, **86**, 011906.

9 X. C. Zhang and D. H. Auston, *Journal of Applied Physics*, 1992, **71**, 326-338.

10 F. R. Bagsican, A. Winchester, S. Ghosh, X. Zhang, L. Ma, M. Wang, H. Murakami, S. Talapatra, R. Vajtai, P. M. Ajayan, J. Kono, M. Tonouchi and I. Kawayama, *Scientific Reports*, 2017, **7**, 1774.

11 T. Mochizuki, A. Ito, J. Mitchell, H. Nakanishi, K. Tanahashi, I. Kawayama, M. Tonouchi, K. Shirasawa and H. Takato, *Applied Physics Letters*, 2017, **110**, 163502.

12 T.-A. Liu, M. Tani, M. Nakajima, M. Hangyo and C.-L. Pan, *Applied Physics Letters*, 2003, **83**, 1322-1324.

13 Q. Li, Z. Tian, X. Zhang, R. Singh, L. Du, J. Gu, J. Han and W. Zhang, *Nature Communications*, 2015, **6**, 7082.

14 N. T. Yardimci and M. Jarrahi, *Small*, 2018, **14**, e1802437.